

Production and Characterization of X-Ray Speckle at Sector 8 of the Advanced Photon Source

A. R. Sandy, L. B. Lurio, and S. G. J. Mochrie
Center for Materials Science and Engineering
Massachusetts Institute of Technology
Cambridge, Massachusetts 02139-4307 USA

A. Malik and G. B. Stephenson
Materials Science Division
Argonne National Laboratory
Argonne, Illinois 60439-4832 USA

M. Sutton
Physics Department
McGill University
Montreal, Quebec H3A 2T8 Canada

ABSTRACT

We have implemented in the undulator first-optics enclosure of the Massachusetts Institute of Technology-McGill University-IBM Corporation Collaborative Access Team Sector at the Advanced Photon Source an x-ray beamline and a spectrometer optimized for performing small-angle, wide-bandpass, coherent-x-ray-scattering experiments. We describe the novel features of this set-up. The performance of the beamline and the spectrometer has been characterized by measuring static x-ray speckle patterns from isotropically-disordered aerogels. Statistical analysis of the speckle patterns has been performed from which we extract the speckle widths and contrast versus wave-vector transfer and sample thickness. The measured speckle widths and contrast are compared to direct numerical evaluations of the intensity correlation function. The calculated widths are in poor agreement with the measurements but the calculated contrast agrees well with the measured contrast.

Keywords: coherent x-ray diffraction, speckle, small-angle x-ray-scattering, aerogel

1. INTRODUCTION

Recent experiments have demonstrated the potential of x-ray intensity-fluctuation spectroscopy (XIFS), which is also known as x-ray photon-correlation spectroscopy (XPCS), to become a powerful probe of sample dynamics at low-frequencies ($< 10^4$ Hz) and small-length-scales (< 2000 Å). For example, XIFS measurements have been made of the equilibrium dynamics of a binary alloy near its critical point,¹ of the Brownian motion of gold,² palladium,³ and antimony oxide⁴ colloids diffusing in glycerol, and of the equilibrium dynamics of block-copolymer micelles in a homopolymer matrix.⁵ All of these measurements were performed in a regime of wave-vector and frequency space which is inaccessible to various other light, neutron, or x-ray scattering techniques.⁶

IFS with laser light has long been employed to investigate the dynamics of condensed matter on micron length scales in transparent media. Its principles are well known: a sample is illuminated by coherent laser light, resulting in a random speckle pattern which varies with time as a result of temporal fluctuations within the sample. The time autocorrelation function of the speckle pattern yields the characteristic times of the sample. Key to performing XIFS, therefore, is a sufficiently coherent x-ray beam illuminating the sample under study. The beam coherence can conveniently be thought of as having two components: (1) transverse or lateral coherence, and (2) longitudinal coherence. The transverse coherence length of the beam is given by $l_T = \lambda R / (\sqrt{2\pi}\sigma)$, where λ is the x-ray wavelength,

Corresponding author: A. R. Sandy, APS/ANL, Sector No. 8, Building 400, 9700 S. Cass Ave., Argonne, IL 60439, USA; email: arsandy@mit.edu; Telephone: 630-252-0280; Fax: 630-252-0282

R is the source-to-observer distance, and σ is the one-sigma source size.⁷ For x-rays produced by our undulator at the Advanced Photon Source (APS), $\lambda \approx 1.6 \text{ \AA}$, $R \approx 30 \text{ m}$, and $\sigma \approx 60 \text{ }\mu\text{m}$ in the vertical direction and $\approx 300 \text{ }\mu\text{m}$ in the horizontal direction yielding transverse coherence lengths at the sample of $l_T \approx 32 \text{ }\mu\text{m}$ in the vertical and $\approx 6 \text{ }\mu\text{m}$ in the horizontal.

The longitudinal coherence length of the beam is given by $l_L = \lambda/(\Delta E/E)$, where E is the energy of the x-ray beam ($\approx 7.6 \text{ keV}$), and ΔE is the energy bandwidth which can range from $\frac{\Delta E}{E} \approx 0.0002$ – 0.05 . In order to observe coherent-scattering effects, the optical path difference of the scattered x-rays must not be too much larger than the longitudinal coherence length of the beam. In fact, for a small-angle-scattering experiment (wave-vector transfers less than approximately 0.05 \AA^{-1}), the energy bandwidth for which coherence effects can be observed is relatively large—a few percent. Recent work in this field has exploited this fact.^{2–5,7,8}

Small-angle coherent-scattering experiments are facilitated in two ways at a third-generation, undulator-based synchrotron-x-ray source. First, the flux of transversely-coherent x-rays is directly proportional to the source brilliance. An undulator at the APS therefore provides approximately a factor of 10^5 more transversely-coherent x-rays through a unit aperture than has been available previously at second-generation synchrotron x-ray sources. Second, the energy bandwidth of an undulator harmonic approximately matches the allowed energy bandwidth of the x-ray beam as derived from optical path-length-difference considerations. Provided that the other undulator harmonics are “filtered” away, it is then possible to use the entire undulator harmonic for a small-angle coherent-scattering experiment with a concomitant increase in flux.

Motivated by these considerations, we have implemented an x-ray beamline and a spectrometer optimized for performing small-angle, wide-bandpass, coherent-x-ray-scattering experiments. Both the beamline and the spectrometer are situated in the undulator first-optics enclosure (FOE) of the IMM-CAT* Sector at the APS. We have incorporated several novel features into the design of our set-up which we describe in detail in Sec. 2.1.

A crucial diagnostic for optimizing our set-up for XIFS measurements is a detailed characterization of its performance under static conditions. This is the main subject of the second half of this paper. In particular, we produce static speckle patterns using isotropically-disordered aerogels and analyze the scattered intensity using a statistical treatment which is described in detail in Ref. [8]. Section 2.2 describes our static structure factor measurements of aerogels and explains why aerogels are excellent canonical static speckle producers. Section 3 details the results of the statistical analysis of the static speckle patterns and Sec. 4 contains a summary and our conclusions.

2. EXPERIMENT

2.1. Beamline configuration

The coherent-scattering measurements described in this paper were carried out at the IMM-CAT Insertion Device Beamline at the APS (8-ID). Table 1 lists distances between various key components in our set-up; Fig. 1 is a schematic plan view of our set-up. From right-to-left in Fig. 1, the principal components are as follows.

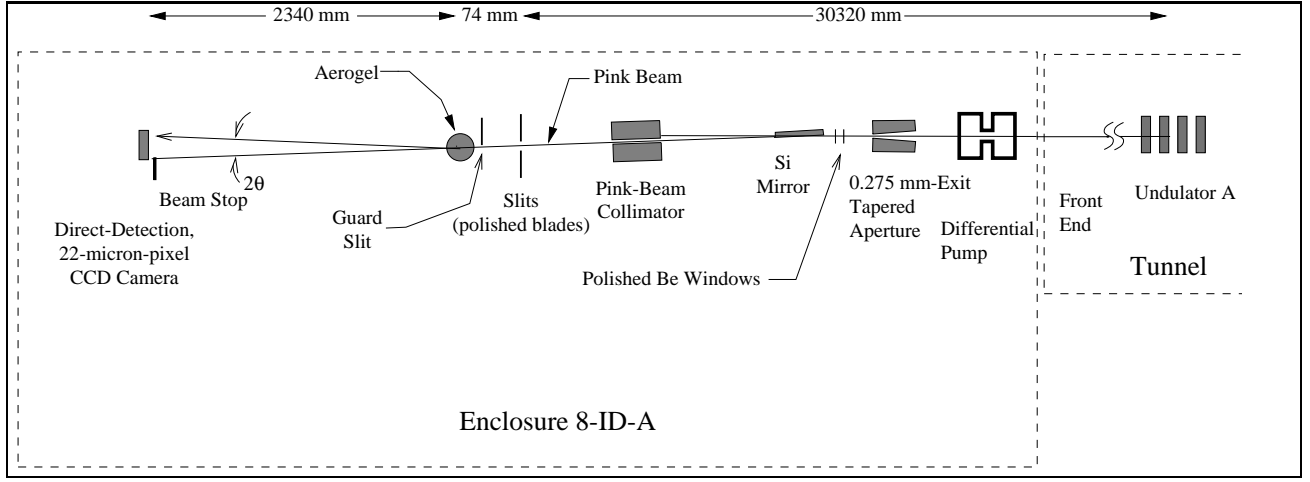
We use an APS Undulator A^{9–11} as our radiation source. It is a 72-pole, 2.4-meter-long insertion device located in the downstream half of the Sector-8 5-meter straight section. The energy range of the undulator first harmonic spans 3–13 keV ($K = 2.57$ – 0.37); we typically run with the undulator gap set to 18.0 mm, which theoretically places the first harmonic at $E = 7.65 \text{ keV}$. The predicted full-width-at-half-maximum (FWHM) bandwidth for the first undulator harmonic is $(\Delta E/E) = 0.026$; the source sizes and x-ray beam divergences at 4% coupling are expected to be $\sigma_x = 300 \text{ }\mu\text{m}$ and $\sigma_{x'} = 25 \text{ }\mu\text{rad}$ in the horizontal and $\sigma_y = 60 \text{ }\mu\text{m}$ and $\sigma_{y'} = 5 \text{ }\mu\text{rad}$ in the vertical.

Radiation propagates from the straight section to our beamline via the APS front end (FE).¹² The FE mates to our beamline via a windowless differential pump. Our differential pump is a modified version of the APS standard model; we added a 30-cm-long tapered aperture with a 3-mm-diameter exit hole between the two halves of the standard differential pump. The tapered aperture serves two purposes. First, it improves the performance of the differential pump by decreasing the gas conductance between its two halves. And second, for our usual undulator gap (18 mm), it reduces the power transmitted to our beamline by a factor of 2 as compared to the FE exit aperture typically supplied by the APS to beamlines.

*IMM-CAT is a team formed to develop a sector at the APS. IMM-CAT is composed of scientists from the Massachusetts Institute of Technology (MIT), McGill and Queen’s Universities in Canada, the International Business Machines Corporation (IBM), and Argonne National Laboratory. To learn more about IMM-CAT, please see <http://www.imm.aps.anl.gov>.

Table 1. Locations of various key components in our small-angle coherent-scattering set-up.

Item	Distance from Source (mm)	Distance from Sample (mm)
Undulator A	0	0
275 μm -Exit-Diameter Aperture	26,988	-3,408
Polished Be Windows (2 \times)	28,630	-1,766
Horizontally-Deflecting Mirror	29,186	-1,210
Collimating Slits	30,322	-74
Guard Slit	30,384	-12
Sample	30,396	0
Beam Stop	32,589	2,193
CCD Detector	32,739	2,343

**Figure 1.** Schematic plan view of our small-angle coherent-x-ray-scattering set-up.

The next component is a tapered aperture with a 275- μm -diameter exit hole. This aperture significantly reduces the total power transmitted to the downstream portion of our beamline to less than 8 W for undulator gaps greater than 18 mm. Since the x-ray beams used in a coherent scattering experiment have transverse dimensions of only 3–20 μm , the small aperture does not compromise in any way the useful transversely-coherent flux. The aperture sits atop a motorized table which allows for precise positioning in the plane transverse (the x - y plane) to the x-ray beam. In practice, we have found that the APS x-ray beam position is stable between and within positron fills, so that once the aperture is placed “on-axis” it rarely needs re-positioning. Immediately upstream and downstream of this aperture, are small-through-bore lead and tungsten collimators. Moreover, the entire aperture itself is wrapped in lead shielding. In this way we greatly reduce the background radiation levels in the FOE.

Downstream of the tapered aperture are two beryllium windows. These isolate the remainder of our beamline from the storage-ring vacuum. Each beryllium window is a highly-polished (both sides), 200- μm -thick beryllium foil clamped to a vacuum flange. Polished beryllium foils have been suggested as important in preserving the beam spatial coherence.¹³ An O-ring formed from a 0.5-mm-diameter lead wire¹⁴ provides vacuum isolation. The beryllium windows do not require cooling because of the small amount of power in the incident beam and because the power is at relatively high x-ray energies so that little is absorbed.

The next component is a horizontally-deflecting, 100-mm-long, silicon mirror. The mirror has less than 5 μrad total slope error across its optical surface and < 5 \AA root-mean-square roughness. The glancing-incidence-angle of the mirror is set so that its critical energy is just greater than the energy of the first undulator harmonic; the

first harmonic of the undulator is reflected and the higher-order harmonics are either absorbed in or transmitted through the mirror. Figure 2 shows the “raw,” measured undulator spectrum (with the gap = 18 mm) after reflection from the mirror—the so-called “pink” beam. We note that the measured profile has the characteristic asymmetric

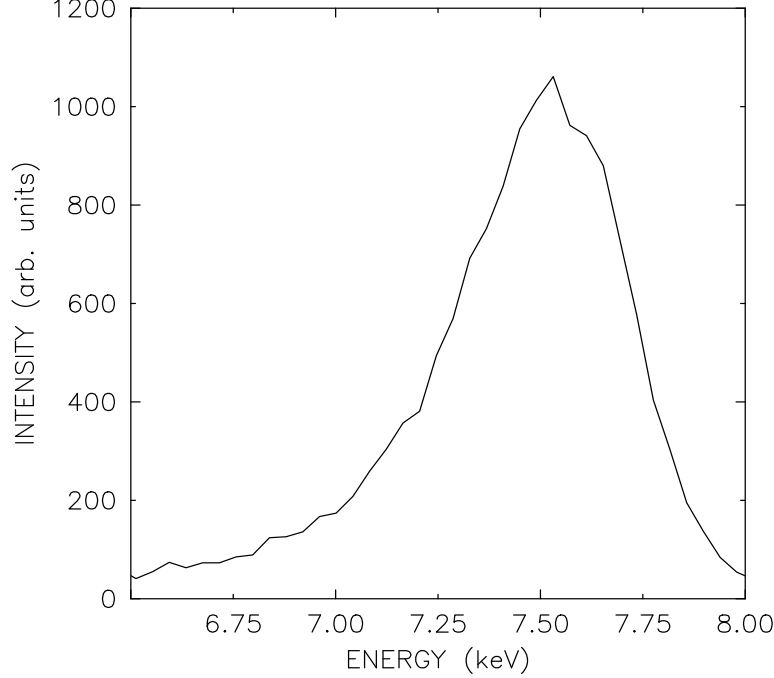


Figure 2. APS Undulator A first harmonic spectrum with the undulator gap set to 18 mm. The measured full-width-at-half-maximum energy bandwidth is $\Delta E/E = 0.059$.

shape of an odd-indexed undulator harmonic, namely, a long low-energy tail and a sharper drop-off on the high-energy side. The spectrum was measured with an Amptek¹⁵ Model XR-100T photodiode x-ray detector. The Amptek’s measured FWHM energy resolution is 317 eV. After deconvolution of the detector resolution, we find the measured FWHM energy bandwidth of the first undulator harmonic is $\Delta E/E = 0.059$, its measured peak position is $E = 7.52$ keV. In addition, the measured count rate of incident photons, scaled to 100 mA of storage-ring current, is 1×10^{15} photons/second. These quantities should be compared to the theoretically-expected values of $\Delta E/E = 0.026$, $E = 7.65$ keV, and an incident count rate of 2×10^{15} photons/second at a storage-ring current of 100 mA. The first two discrepancies could result from one of our apertures not being properly aligned on the axis of the beam,¹¹ while the last probably just reflects the uncertainty of our flux measurement.

The remaining items in our set-up constitute the small-angle coherent-scattering spectrometer. These components are located atop two movable tables which will be relocated to downstream experiment stations upon the latter’s completion. The first component that is part of the spectrometer is a second small-through-bore lead collimator. In the current set-up it sits approximately 600-mm downstream of the mirror. This collimator is aligned so that the reflected pink beam passes through it while any high-energy radiation transmitted through the mirror is absorbed.

The next item in the small-angle coherent-scattering spectrometer is a pair of crossed slits used to select a transversely coherent portion of the x-ray beam. The slit assembly is a custom design which allows the slit blades to be placed within 7.5 cm of the sample. The small slit-to-sample separation allows us to work in the near-field limit (Fresnel diffraction) of the slits for all but the smallest slit apertures. Otherwise, we have found that the contrast in the speckle pattern (see Sec. 3) is reduced by the divergence of the x-ray beam between the slit and the sample. The slit blades are made of tantalum and their beam-defining edges are polished to reduce parasitic scattering. The slits have independent adjustable openings in the horizontal and vertical directions from $\approx 1 \mu\text{m}$ to several mm. Independent horizontal and vertical apertures allow us to choose slit openings that best match the different horizontal and vertical source sizes. The resolution and repeatability of the slit apertures and positions are $\approx 0.2 \mu\text{m}$ and \approx

1 μm , respectively. For the coherent-scattering data presented in this paper the slit apertures were 5 μm in the horizontal \times 11 μm in the vertical. The measured count rate incident upon the sample and scaled to 100 mA of storage-ring current was 1×10^{12} photons/second, which is a factor of two less than expected, but consistent with our measurements of the count rate through the 275- μm aperture. The mirror, collimator, and slits are all contained within a He-filled flight path. The beam defined by the slits exits the incident flight path through a small hole in a Kapton window at the end of this portion of the flight path. We use a hole to avoid complications which we have otherwise observed to result from the Kapton decomposing in the intense x-ray beam.

The samples we studied were contained in a small vacuum chamber. The x-ray beam entered the chamber via a Kapton window. Unlike the Kapton window described above which is exposed to the entire 275- μm x-ray beam during alignment and beam characterization, this window only “sees” micron-sized x-ray beams. We have found that such a small beam produces very little damage in the window. The downstream end of the chamber was directly connected to the detector flight path. Immediately upstream of the sample, and inside the chamber, was a guard slit made of polished tantalum foil. It was used to reduce the parasitic scattering produced by the slits and the sample-chamber’s Kapton window. We used only a single slit and mounted it on the inboard (storage-ring) side of the beam with its edge vertical. Likewise, the CCD camera (see below), was mounted so that it only collected scattering in the inboard direction. By working only in the inboard half-plane, we have greatly simplified the alignment of the guard slit. This has proven especially valuable for dynamics measurements we have made with this same set-up where frequent sample and temperature changes necessitate frequent re-alignment of the guard slit.

A Princeton Instruments¹⁶ Model CCD-576E, thermo-electrically-cooled, deep-depletion CCD chip with 384×576 22- μm -square pixels directly detected the intensity scattered from the aerogel samples. Its quantum efficiency at the x-ray energy we used was about 35%. The camera was controlled by and the data stored on a Silicon Graphics workstation using a customized version of the “Yorick” interpreted programming language.¹⁷ Data presented in this paper are the average of between 10 and 25 CCD exposures, each of duration 0.4 to 1.0 seconds. Readout time between each of the exposures was 0.24 seconds. Obtaining data as a time series has two advantages: (1) it allows the CCD performance to be characterized as described in Ref. [18], and (2) it allows for tests of the stability of our experimental configuration.

The CCD was protected from the direct x-ray beam by a beamstop made of copper. Both the beamstop and the guard slit are movable *in situ*, so by observing in real time the scattered intensity recorded by the CCD, we were able to optimize the positions of these items in order to minimize the parasitic contribution to the measured scattering.

2.2. Aerogel samples

The aerogel samples used in the present study were made via a sol-gel and supercritical drying process,¹⁹ resulting in a highly porous material composed of SiO_2 spheres arrayed in long strands interconnected at random sites. Depending on the growth conditions, gels with varying density could be produced. For the present measurements the density and thickness of the gels were varied so that each sample comprised approximately one x-ray absorption length.

X-ray-scattering measurements of the aerogel ensemble-averaged static structure factors were made at MIT-IBM Beamline X20C at the National Synchrotron Light Source. Approximately 4 mrad of synchrotron radiation from a bending magnet were collected and focused by a platinum-coated, bent, cylindrical, float-glass mirror. Monochromatic x-rays of energy $E = 7.1$ keV were selected by a pair of tungsten-silicon multilayers. At the sample position, we obtained on the order 1×10^{13} photons/second at 100 mA ring current in a bandwidth $\Delta E/E = 0.015$ and a spot size approximately 1×1 mm². A pair of crossed slits upstream of the sample provided collimation of the incident beam. An additional crossed slit, immediately upstream of the sample, was used to remove parasitic scattering from the upstream slits and windows. The scattered intensity was collected using a “point” scintillation detector mounted on a vertically-scanning detector arm. Crossed slits on the upstream and downstream end of the detector arm determined our resolution and minimized the contribution of parasitic scattering to the measured signal.

The static x-ray scattering from aerogels has been extensively studied and is well understood.^{20–22} On length scales of a few hundred angstroms, the strands cluster into a fractal network with fractal dimension close to 2. This structure leads to strong x-ray scattering over a wide range of wave-vector transfers and makes the gels useful in characterizing coherence. At length scales beyond the cluster size, different clusters pack together. Viewed at still larger length scales, their density appears uniform and the fractal dimension approaches 3.

Figure 3 shows the measured scattering from a 3.4-mm-thick aerogel (open circles). The data have been normalized to the scattering per unit volume. Also shown in Fig. 3 is a best fit (solid line) to the measured scattering based on the model described in detail in Ref. [21]. This model represents the total scattering as the product of three terms:

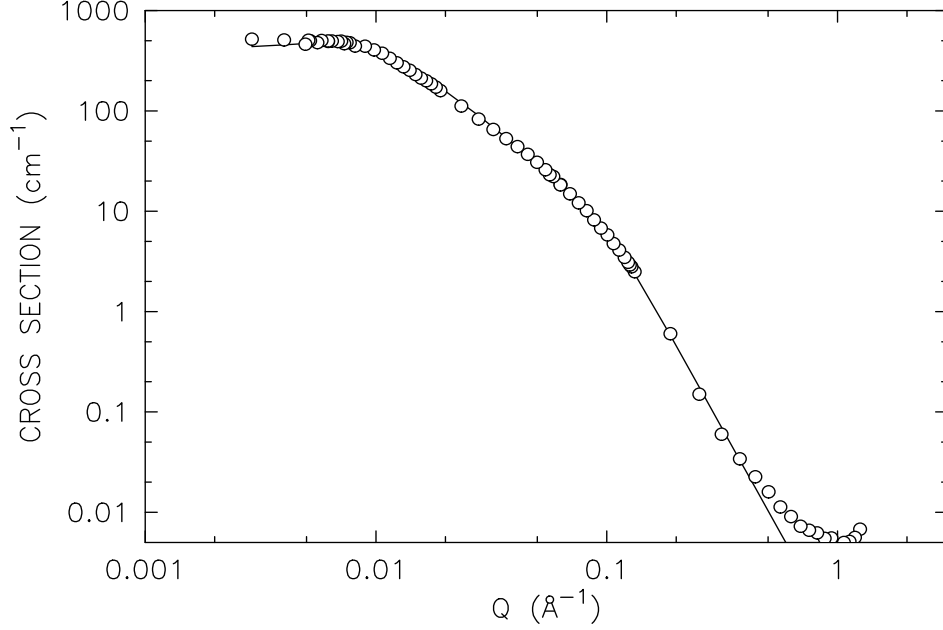


Figure 3. Measured and calculated scattering from a 3.4-mm-thick, 0.0287 g/cm³, silica aerogel. Open circles are data and the solid line is the best fit by the model described in the text. The upturn in the data at large Q results from the silica inter-molecular spacing (~ 2 Å), which is not included in the model.

$$S(Q) = \left[\frac{1}{1 + \frac{2}{9}Q^4 R^4} \right] \left[1 + \frac{1}{(QR)^{d_f}} \frac{d_f \Gamma(d_f - 1) \sin[(d_f - 1) \tan^{-1}(Q\xi)]}{(1 + 1/(Q^2 \xi^2))^{(d_f - 1)/2}} \right] \left[\Theta(QD) \frac{1}{1 + 8p\Theta(QD)} \right].$$

The first term represents the scattering from individual silica spheres of average radius R^\dagger . The second term represents scattering from the fractal regions of cluster size D with fractal dimension d_f and fractal correlation length ξ . Γ is the gamma function. The third term represents the packing of the clusters with packing fraction p . Here Θ is the scattering form factor for a sphere.

Aerogels of varying density could all be reasonably well described by this model. Fits to the entire collection of aerogel scattering profiles were done with the same silica-sphere radius. From the fit results we find that as the density of the gels increased, the cluster size and the correlation length decreased with a corresponding increase in the packing fraction and the fractal dimension. For the data presented in Fig. 3, the best-fit parameters are $p = 0.02$, $D = 736$ Å, $\xi = 121$ Å, $d_f = 2.1$, and $R = 15$ Å.

3. STATIC SPECKLE PATTERN ANALYSIS

Three aerogel speckle patterns are shown in Fig. 4. From left to right, Fig. 4 shows the small-angle scattering from 0.5-mm-thick, 1.0-mm-thick, and 3.4-mm-thick aerogel samples. For all the images presented in Fig. 4, dark regions indicate more recorded scattering and light regions indicate less. Data presented for the 0.5-mm-thick aerogel sample are the average of 25 0.4-second CCD exposures, those presented for the 1.0-mm-thick aerogel sample are the average of 25 0.5-second CCD exposures, while those presented for the 3.4-mm-thick aerogel sample are the average of 10 1.0-second CCD exposures. For all three images the scattered signal was diminished by an $\approx 100\times$ attenuator

[†]Due to the distribution in size of the silica spheres, this term is simply Porod scattering. It is independent of the detailed shape of the silica particles and the value of the average radius serves only to determine the total surface area.

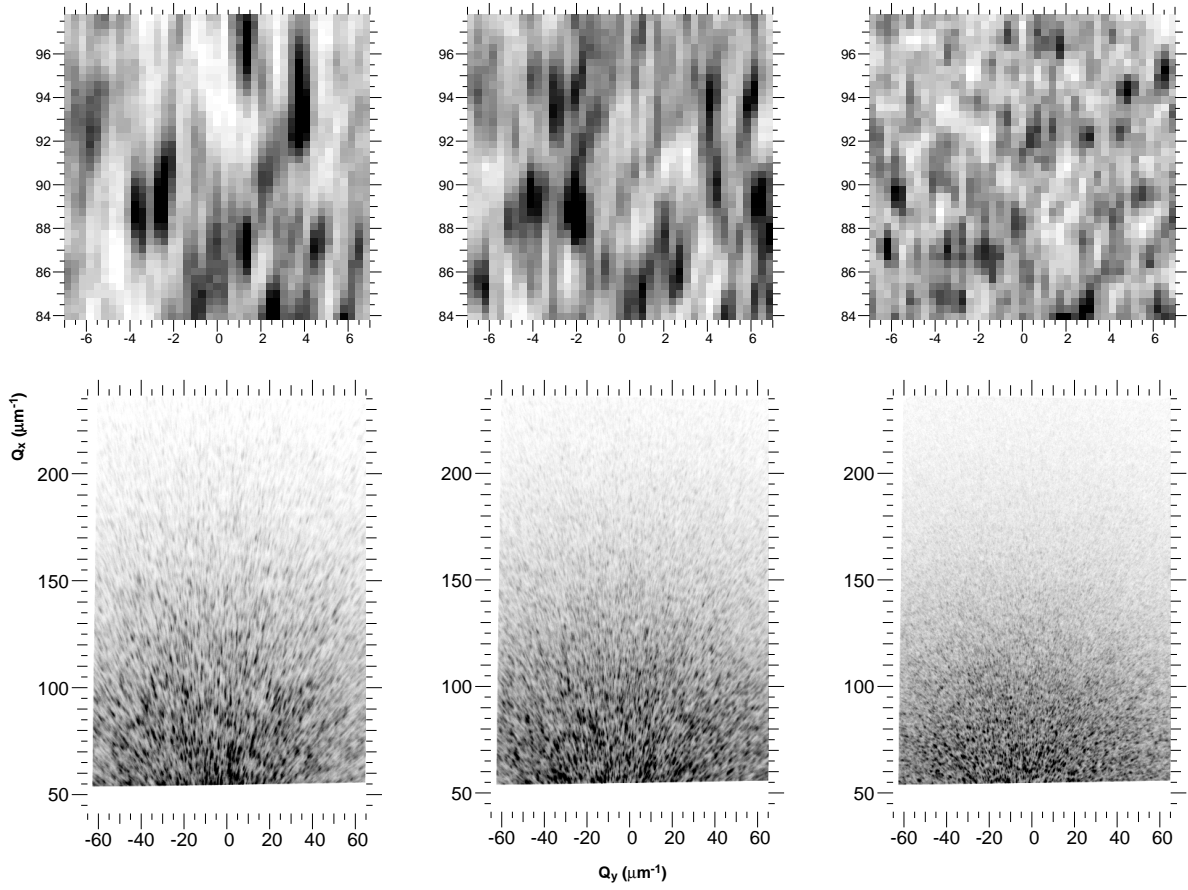


Figure 4. Speckle patterns produced by a wide-bandpass coherent x-ray beam incident upon aerogel samples of varying thicknesses. Left Panels: scattering from a 0.5-mm-thick aerogel sample. Center Panels: scattering from a 1.0-mm-thick aerogel sample. Right Panels: scattering from a 3.4-mm-thick aerogel sample. The bottom panel of each pair of figures is the entire CCD image, the top panel is a close-up in the range of \vec{Q} indicated. The white band at the bottom of all three of the entire CCD images is the shadow of the beam stop.

immediately upstream of the CCD in order to avoid saturation. All the data presented in Fig. 4 have been converted to wave-vector transfer (\vec{Q}) using the relation $\vec{Q} = k\vec{r}/R_d$, where $k = 2\pi/\lambda = 3.88 \text{ \AA}^{-1}$ is the wave number, \vec{r} is a vector from a point on the CCD image plane to the beam-zero position on the CCD image plane, and R_d is the separation between the sample and the detector (see Table 1). The direct beam (stopped by a beam stop) is at $|\vec{Q}| = Q = 0$, Q_x is in the horizontal direction, and Q_y is in the vertical direction.

There are several notable qualitative features apparent in Fig. 4. First, for all three patterns the measured scattering is grainy—this is speckle! Second, we observe that with increasing wave-vector transfer and sample thickness, the longitudinal widths of the speckles appear to decrease. The decrease of speckle size with sample thickness is especially apparent when we compare the speckle-pattern close-up for the 0.5-mm-thick aerogel (top left panel of Fig. 4) with the speckle-pattern close-up for the 3.4-mm-thick aerogel (top right panel of Fig. 4). Finally, the fact that there is speckle at all demonstrates that our set-up does result in a partially coherent x-ray beam incident upon the sample.

In order to quantify these observations, we turn to a statistical analysis of the static x-ray speckle patterns. We omit detailed explanations of the formalism of this method as it has recently been presented by Abernathy *et al.* in Ref. [8]. A similar analysis has also recently been presented in Ref. [7]. The analysis presented by Abernathy *et al.* incorporates results obtained from laser-light scattering for the effects of partially-coherent beams, energy bandpass, and source and detector sizes on measured speckle patterns.²³

The speckle patterns are analyzed as follows. First the detector response is characterized by calculating the spatial autocorrelation of each CCD frame in a region where the measured intensity is very weak (isolated photon “hits”),¹⁸ in order to determine the spatial resolution of the detector independent of complicating intensity variations due to the speckle pattern itself. From this analysis we find that the FWHM detector resolution is 1.1 pixels or $0.4 \mu\text{m}^{-1}$ in both the vertical and horizontal directions.

Key to the remainder of the analysis is the two-point intensity correlation function:

$$C(\vec{r}_1, \vec{r}_2) = \frac{\langle I(\vec{r}_1)I(\vec{r}_2) \rangle}{\langle I(\vec{r}_1) \rangle \langle I(\vec{r}_2) \rangle} \quad (1)$$

where the \vec{r}_i are points in the CCD image-plane, and the angle brackets indicate a spatial average over a suitable region of the time average of a series of CCD frames. The spatial autocorrelation function is maximized for $\vec{r}_1 = \vec{r}_2$ [$1 \leq C(\vec{r}, \vec{r}) \leq 2$], while for large separations it decays to 1. The contrast of the speckle pattern—an important figure-of-merit for a coherent scattering experiment—is the background subtracted value of the maximum of the spatial autocorrelation function, $\beta(\vec{r}) = C(\vec{r}, \vec{r}) - 1$; the FWHM’s of the background-subtracted intensity-correlation function, $C(\vec{r}_1, \vec{r}_2) - 1$, yield the speckle widths. As an example, Fig. 5 shows the intensity autocorrelation calculated over the 0.5-mm-thick aerogel speckle pattern close-up (top left panel) in Fig. 4. Open circles are data in the

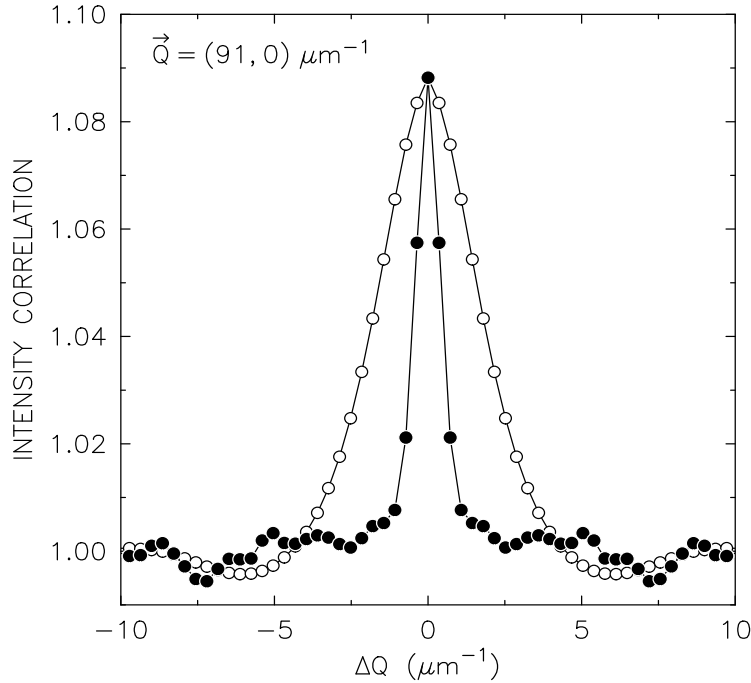


Figure 5. Intensity autocorrelation in the Q_x (open circles) and Q_y (solid circles) directions for the 0.5-mm-thick aerogel speckle pattern close-up (top left panel) in Fig. 4. Solid lines are guides-to-the-eye. One μm^{-1} is equal to 2.7 pixels.

longitudinal (Q_x) direction and solid circles are data in the transverse (Q_y) direction. Evidently, the speckles are considerably broader in the longitudinal direction than in the transverse direction. This can also be seen by inspection of the top left panel of Fig. 4.

Figure 6 shows the measured speckle FWHM’s versus wave-vector transfer for the three aerogel speckle patterns presented in Fig. 4. The longitudinal widths have been measured in the vicinity of the horizontal plane passing through $Q = 0$ [$(Q_x, 0)$ in Fig. 4], and the transverse widths are orthogonal to this direction. The transverse speckle widths (solid symbols) for all three samples thicknesses are relatively small and appear to be independent of Q ; the longitudinal speckle widths (open symbols) are relatively large (except for the thickest sample) and seem to

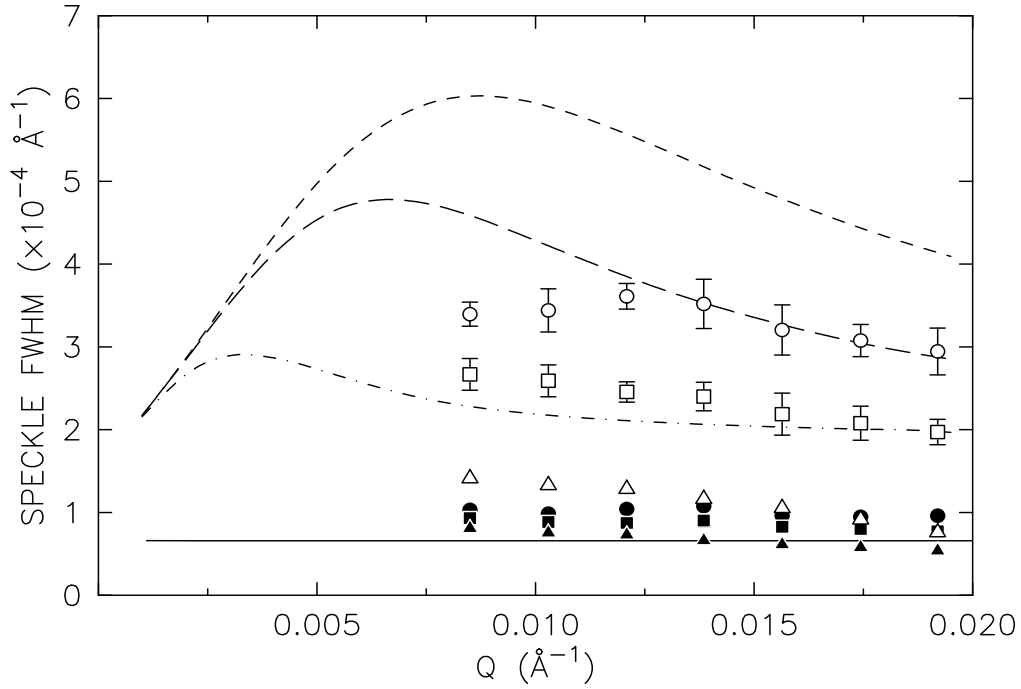


Figure 6. Speckle widths versus wave-vector transfer for the speckle patterns presented in Fig. 4. Open symbols are longitudinal widths and solid symbols are transverse widths. Circles are data for the 0.5-mm-thick sample, squares are data for the 1.0-mm-thick sample, and triangles are data for the 3.4-mm-thick sample. Solid, dashed and dash-dotted lines are model predictions (explained in the text) for the results from the 0.5-mm-thick sample, the 1.0-mm-thick sample, and the 3.4-mm-thick sample, respectively.

vary weakly with Q . In particular, at larger Q , for all three samples, the longitudinal speckle widths decrease with increasing Q .

The variation of the longitudinal speckle width versus Q for a particular sample thickness can be intuitively understood by considering the 2 contributions to the effective slit size versus Q as seen at the detector. The first effect is the foreshortening of the slit aperture with increasing scattering angle which leads to a quadratic increase in the longitudinal speckle width with increasing Q . The second effect results from the apparent increase in sample thickness with increasing Q . The effective sample thickness is proportional to an effective slit width which leads to a $1/Q$ -dependence for the speckle width versus increasing Q . The first effect dominates at small Q and the second at larger Q . We also note that the first effect is independent of the sample thickness while the second is not and predicts that thicker samples yield narrower speckles. In this way we can understand the overall decrease in the longitudinal speckle widths with increasing sample thickness which is observed in Fig. 6.

Figure 7 shows the measured contrast for the 3 aerogel speckle patterns. For all three samples the measured contrast decreases continuously with increasing Q . In addition, we see that the contrast decreases for successively thicker samples.

In order to model the observed speckle widths and contrast, we turn to a theoretical treatment of partial coherence and x-ray scattering. Several authors have written papers on this subject recently.^{7,8,24,25} We choose to apply a theory⁸ which has been developed for analyzing exactly the measurements presented in this section. In this theory, the intensity correlation function [Eq. (1)] is written as convolutions of the complex coherence factor $[\mu(k, k', \vec{r}, \vec{r}')]$ over the wave-number spread, the detector resolution, and the source-size contributions:

$$C(\vec{r}_1, \vec{r}_2) - 1 = \int \mathcal{W}(k) \mathcal{W}(k') R(\vec{r}_1 - \vec{r}') R(\vec{r}_2 - \vec{r}'') \Sigma(\vec{r}' - \vec{r}''') \Sigma(\vec{r}'' - \vec{r}''') |\mu(k, k', \vec{r}', \vec{r}''')|^2 dk dk' d\vec{r}' d\vec{r}'' d\vec{r}''' d\vec{r}'''' \quad (2)$$

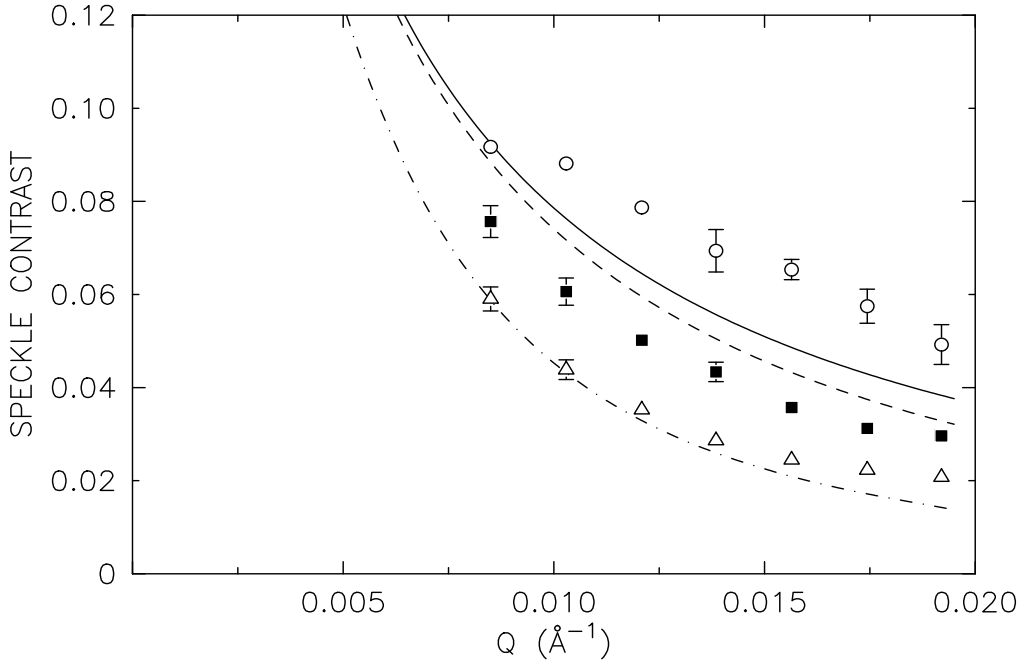


Figure 7. Contrast versus wave-vector transfer for the speckle patterns presented in Fig. 4. Open circles are data for the 0.5-mm-thick sample, solid squares are data for the 1.0-mm-thick sample, and open triangles are data for the 3.4-mm-thick sample. Solid, dashed and dash-dotted lines are model predictions (explained in the text) for the results from the 0.5-mm-thick sample, the 1.0-mm-thick sample, and the 3.4-mm-thick sample, respectively.

with the complex coherence factor for partially-coherent radiation given by

$$\mu(k, k', \vec{r}, \vec{r}') = \int |B(\vec{\rho})|^2 e^{i(\vec{Q}(k, \vec{r}) - \vec{Q}(k', \vec{r}')) \cdot \vec{\rho}} d\vec{\rho}. \quad (3)$$

In Eqs. (2) and (3), $\mathcal{W}(k)$ is the normalized wave-number distribution, $R(\vec{r})$ is the normalized detector resolution, $\Sigma(\vec{r})$ is the source-size contribution, $B(\vec{\rho})$ is the incident radiation field and is assumed to be a constant over the slit aperture and zero otherwise, \vec{r} is a point in the CCD image plane, and $\vec{\rho}$ is a point in the sample volume. The source-size contribution is included as a convolution over the detector plane with the source size scaled by the ratio of the detector-sample to the sample-source distances.⁸

Using box functions for the slit sizes, sample thicknesses, and detector resolution; Gaussians for the source profile; and the normalized, deconvolved, measured profile of the first harmonic of the undulator (see Fig. 2) for the wave-number distribution, we have directly evaluated Eqs. (2) and (3) to obtain the speckle widths and contrast versus wave-vector transfer. The calculated results for the transverse speckle widths are plotted as a solid line in Fig. 6. The transverse speckle width is predicted to be independent of the aerogel thickness and wave-vector transfer in good agreement with the data. However, with no adjustable parameters, the calculations are seen to somewhat underestimate the measured widths.

The calculated longitudinal speckle widths versus Q are shown as short-dashed, long-dashed, and dot-dashed lines in Fig. 6 for the 0.5-mm-thick, 1.0-mm-thick, and 3.4-mm-thick aerogel samples, respectively. As for the transverse widths described above, no adjustable parameters are used in the calculations. For all three samples, the calculations predict significantly greater widths than are observed. The discrepancy arises from the source-size terms in the integrand of Eq. (2), which may indicate that either source-size effects have not been properly included in deriving Eqs. (2) and (3) or that in the horizontal direction, at least, the source is not well-described by a Gaussian. The calculations also seem to predict more Q -dependence to the longitudinal widths than we observe. We have found, however, that using a normalized wave-number distribution derived from the theoretical undulator spectrum as opposed to our measured undulator spectrum ($\Delta E/E = 0.026$ versus 0.059), produces a speckle-width

Q -dependence that more closely resembles our data. Even when using the theoretical undulator spectrum, however, we still find that the predicted speckle widths are significantly larger than the measured speckle widths.

We have also determined the expected contrast in the speckle pattern via evaluation of Eq. (2). The predicted contrast versus Q for the various aerogel samples agrees well with the observed contrast. This is shown by the solid (0.5-mm-thick aerogel), dashed (1.0-mm-thick aerogel), and dot-dashed (3.4-mm-thick aerogel) lines in Fig. 7 which are the numerically-evaluated values of the contrast using Eq. (2).

4. CONCLUSIONS

We have implemented a beamline and a spectrometer specialized to performing small-angle coherent-scattering experiments. The entire set-up is located in the undulator FOE of the Massachusetts Institute of Technology-McGill University-IBM Corporation Collaborative Access Team Sector at the APS. Using 2 small-exit-diameter apertures, we have been able to vacuum integrate our beamline with the APS storage ring, reduce the background radiation-level in the FOE so that experiments are feasible there, and reduce the power in the x-ray beam to a manageable level. A small horizontally-deflecting mirror is used to isolate the first harmonic of the undulator from the “white” incident spectrum and produce a pink beam incident upon the small-angle coherent-scattering spectrometer. The spectrometer illuminates the sample under study with a transversely-coherent x-ray beam and records the scattered intensity via a CCD detector.

We have used this set-up to measure static speckle patterns from 3 aerogel samples of varying thicknesses. The static speckle patterns have been analyzed using a statistical approach from which we obtain the speckle widths and contrast versus wave-vector transfer. The results have been compared to direct numerical evaluations of the intensity correlation function. Predicted speckle widths are in poor agreement with the observed widths for all the samples studied. This discrepancy may arise because the effect of source smearing has not been properly included in the expression for the intensity correlation function or because a Gaussian is a poor approximation to the source profile. We do find, however, that the predicted speckle contrast agrees very well with the observed values. We conclude that our set-up is performing at close to its optimum level.

Finally, in conclusion we note that in Ref. [8], Eqs. (2) and (3) are greatly simplified by making a series of Gaussian approximations to the slit sizes, the sample thickness, and the energy bandwidth of the incident radiation. Then, with some additional minor assumptions,⁸ the contrast and speckle widths versus wave-vector transfer can be written in closed form. These expressions are quite useful for predicting trends in the measured data. We have found, however, by substituting these approximations one-by-one into our evaluations of Eqs. (2) and (3), that the Gaussian approximation to the undulator harmonic produces significantly greater predicted contrast than the real undulator spectrum. Presumably this is because a Gaussian does not adequately model the asymmetric shape of the undulator harmonic. The Gaussian approximation may, however, be suitable for modeling the energy spectrum produced by a multilayer.⁷

ACKNOWLEDGEMENTS

We thank Douglas Abernathy and Gerhard Grübel of the European Synchrotron Radiation Facility, Mohan Ramanathan and Wenbing Yun of the APS, and Ophelia Tsui of MIT for illuminating conversations. We appreciate the craftsmanship of Frank DePaola and Central Shops at Argonne National Laboratory and, in particular, the tremendous skill and effort they invested in constructing the 275- μ m-exit-diameter UHV aperture. We also acknowledge Prof. N. Mulders for supplying the aerogel samples used in this work. We are especially grateful to Douglas Abernathy for providing many of the “Yorick” routines that were used as the basis for the speckle analysis presented here and Wenbing Yun for the loan of the mirror. Lastly, we acknowledge support under NSF grant DMR-9312543 to MIT which provided the major funding for the implementation described here. Additional funding was provided by NSERC.

REFERENCES

1. S. Brauer, G. B. Stephenson, M. Sutton, R. Brünig, E. Dufresne, S. G. J. Mochrie, J. Als-Nielsen, G. Grübel, and D. L. Abernathy, “X-ray intensity fluctuation spectroscopy observations of critical dynamics in Fe_3Al ,” *Phys. Rev. Lett.* **74**, pp. 2010–2013, 1995.

2. S. B. Dierker, R. Pindak, R. M. Fleming, I. K. Robinson, and L. Berman, "X-ray photon correlation spectroscopy study of brownian motion of gold colloids in glycerol," *Phys. Rev. Lett.* **75**, pp. 449–452, 1995.
3. T. Thurn-Albrecht, W. Steffen, A. Patkowski, G. Meier, E. W. Fischer, G. Grübel, and D. L. Abernathy, "Photon correlation spectroscopy study of colloidal palladium using a coherent x-ray beam," *Phys. Rev. Lett.* **77**, pp. 5437–5440, 1996.
4. O. K. C. Tsui and S. G. J. Mochrie, "Dynamics of concentrated colloidal suspensions probed by x-ray correlation spectroscopy." preprint.
5. S. G. J. Mochrie, A. M. Mayes, A. R. Sandy, M. Sutton, S. Brauer, G. B. Stephenson, D. L. Abernathy, and G. Grübel, "Dynamics of block copolymer micelles revealed by x-ray intensity fluctuation spectroscopy," *Phys. Rev. Lett.* **78**, pp. 1275–1278, 1997.
6. S. Dierker, "X-ray photon correlation spectroscopy at the NSLS." NSLS Newsletter, July 1995.
7. O. K. C. Tsui, S. G. J. Mochrie, and L. E. Berman, "Statistical analysis of x-ray speckle at the NSLS." preprint.
8. D. L. Abernathy, S. Brauer, G. Grübel, I. McNulty, S. G. J. Mochrie, N. Mulders, A. R. Sandy, G. B. Stephenson, and M. Sutton, "Small-angle coherent x-ray scattering using undulator radiation at the ESRF." *J. Synch. Rad.* (to be published).
9. B. Lai, A. Khounsary, R. Savoy, L. Moog, and E. Gluskin, "Undulator A characteristics and specifications," Tech. Rep. ANL/APS/TB-3, Argonne National Laboratory, 1993.
10. R. J. Dejus, B. Lai, E. R. Moog, and E. Gluskin, "Undulator A characteristics and specifications: Enhanced capabilities," Tech. Rep. ANL/APS/TB-17, Argonne National Laboratory, 1994.
11. P. Illinski, R. J. Dejus, E. Gluskin, and T. I. Morrison, "Some practical aspects of undulator radiation properties," in *Optics for High-Brightness Synchrotron Radiation Beamlines II*, L. E. Berman and J. R. Arthur, eds., *Proc. SPIE* **2856**, pp. 16–25, 1996.
12. T. Kuzay, "Functional description of APS beamline front ends," Tech. Rep. ANL/APS/TB-5, Argonne National Laboratory, 1993.
13. A. Snigirev, I. Snigireva, V. G. Kohn, and S. M. Kuznetsov, "On the requirements to the instrumentation for the new generation of the synchrotron radiation sources: Beryllium windows," *Nucl. Instr. and Meth.* **A370**, pp. 634–640, 1996.
14. T. Oversluizen and P. M. Stefan, "Replaceable Be and Al windows for x-ray beamlines," *Nucl. Instr. and Meth.* **A266**, pp. 375–380, 1988.
15. Amptek Inc., Bedford, Massachusetts, USA.
16. Princeton Instruments Inc., Trenton, New Jersey, USA.
17. D. H. Munro, "Using the Yorick interpreted language," *Comp. Phys.* **9**, pp. 609–615, 1995.
18. E. Dufresne, R. Brüning, M. Sutton, B. Rodricks, and G. B. Stephenson, "A statistical technique for characterizing x-ray position-sensitive detectors," *Nucl. Instr. and Meth.* **A364**, pp. 380–393, 1995.
19. J. Fricke, ed., *Aerogels*, Springer-Verlag, Berlin, 1984.
20. R. Vacher, T. Woignier, J. Pelous, and E. Courtens, "Structure and self-similarity of silica aerogels," *Phys. Rev. B* **37**, pp. 6500–6503, 1988.
21. D. Posselt, J. S. Pedersen, and K. Mortensen, "A SANS investigation on absolute scale of a homologous series of base-catalysed silica aerogels," *J. Non-Cryst. Sol.* **145**, pp. 128–132, 1992.
22. J. Teixeira, "On growth and form," in *NATO ASI E-100*, H. Stanley and N. Ostrowsky, eds., p. 145, Nijhoff, Dordrecht, 1988.
23. J. C. Dainty, ed., *Laser Speckle and Related Phenomena*, Springer-Verlag, Berlin, 1984.
24. S. K. Sinha, M. Tolan, and A. Gibaud, "The effects of partial coherence on the scattering of x-rays by matter." preprint.
25. B. Lin, M. L. Schlossman, M. Meron, S. M. Williams, Z. Huang, and P. J. Viccaro, "X-ray speckles from an optical grating." preprint.